Science Advances
AAAS

Supplementary Materials for

A unified perspective of seismicity and fault coupling along the San Andreas Fault

Yuan-Kai Liu*, Zachary E. Ross, Elizabeth S. Cochran, Nadia Lapusta

*Corresponding author. Email: ykliu@caltech.edu

Published 23 February 2022, *Sci. Adv.* **8**, eabk1167 (2022)
DOI: 10.1126/sciadv.abk1167

This PDF file includes:

Materials and Methods
Supplementary Text
Figs. S1 to S8
References

Materials and Methods

Data:

The dataset used in this work is the Northern California Seismic Network double-difference (DD) earthquake catalog (*15, 56, 57*). The automatic and routinely relocated earthquake catalog was downloaded from the Northern California Earthquake Data Center. The catalog covers events of the entire central and northern California since January of 1984 to February of 2021. We further select a subset of this catalog along the strike of the 225-km-long central San Andreas Fault (central SAF) extending from around Loma Prieta in the northwest (122.25°W, 37.40N) to near the Carrizo segment in the southeast (120.14°W, 35.59°N) within ± 5 km distance from the fault. The majority of the hypocenters locate at around 2 to 8 km depth (Fig. S1). To include the deeper events from the 1989 Loma Prieta sequence which sit on a dipping fault plane, we increase the width of our data selection to ± 10 km for the region north of San Juan Bautista.

The regions further north of the Loma Prieta and further south of Cholame (the Carrizo segment) are dominated by rarely occurring historic large mainshocks and aftershocks. These include the 1857 M7.9 Fort Tejon earthquake (*58*) in the south, 1906 M7.9 San Francisco earthquake (*59*) in the north. The above segments at the both ends of our study profile have insufficient events during periods devoid of large shocks for interevent-time analysis and thus can easily lead to overestimation of the fraction of non-clustered seismicity due to the sampling bias

(*32*). We hereby exclude these portions of the central SAF from our discussion.

Magnitude of completeness estimation:

The magnitude of the catalog is duration magnitude (M_d). We assess the magnitude of completeness (M_c) using the maximum curvature (MAXC) method (*60*). This method defines the point of the maximum curvature as the magnitude of completeness by computing the maximum value of the first derivative of the frequency-magnitude distribution curve. In practice, it is equivalent to the magnitude bin with the highest frequency of events in the non-cumulative frequency-magnitude distribution. Since the MAXC technique tends to slightly underestimate the magnitude of completeness, we add 0.2 for correction (*61*). Based on the selected subset of the catalog, we estimate M_c for every year from 1984 to 2021 and find that the values are within the range of 0.8–1.5 (Fig. S2). We thus set a constant minimum magnitude M_{min}=1.5 for the entire analysis, which results in 24,082 events over 37 years (Fig. S3). With this subset catalog, we apply a moving spatial window along the fault (15 km along-strike by 10 km fault-normal, step size 1 km) and compute properties of seismicity within the spatial window. We also make sure that, within each window, there are more than 1,000 events larger than M_c. The computed seismicity properties, including b-values, non-clustered seismicity rate, and fraction of non-clustered seismicity, are described in the following sections.

b-value estimation:

We estimate the b-value of the dataset with the maximum likelihood method proposed by Aki (*62*), where, for each subset of events within the spatial window, the b-value is computed as:

$$b = \frac{log_{10}(e)}{\overline{M} - M_{min}}$$

where e is the Euler's number, $\overline{M}$ is the mean magnitude of the seismicity, and $M_{min} = 1.5$

is the chosen cutoff magnitude. The estimated b-values in our dataset range from 0.6 to 1.2 along the central SAF.

Non-clustered seismicity rate and fraction of non-clustered seismicity:

Under the framework of Epidemic-type Aftershock-sequences Model (*51, 63, 64*), we assume that the earthquake catalog is composed of two types of events in terms of temporal clustering behavior: one is the clustered seismicity which is triggered by other events and their occurrences follow the Omori law (*54, 64*). The other type is the non-clustered seismicity which are independent from each other and follows the homogeneous Poisson process. The former is equivalent to aftershocks, while the later represents the background seismicity. Our analysis in the main text is based on the fraction of non-clustered seismicity in the earthquake catalog. Based on the mild assumptions that general seismicity has Poissonian non-clustered events superimposed with triggered aftershocks that follow the Omori law, it has been shown that the non-clustered seismicity rate could be estimated with methods based on the distribution of waiting times (interevent times), Δt, between consecutive earthquakes (*65*) proposed that the probability density function of interevent times of general seismicity can be approximated as a Gamma distribution:

$$P(\Delta t) = C \cdot^{\gamma-1} \cdot \exp^{-\Delta t \mu}$$

i.e.,

$$\Delta t \sim \Gamma(\gamma, \mu)$$

where C is a normalization constant, μ is the non-clustered seismicity rate, and γ is a model parameter. The Gamma distribution, $\Gamma(\gamma, \mu)$, is assumed to be flexible enough to capture a range of behavior that the interevent times of seismicity could exhibit. Molchan (*52*) and Hainzl et al. (*41*), based on the theoretical analysis, further showed that the non-clustered seismicity rate, μ, can be estimated from the first two sample moments of the interevent times:

$$\mu = \frac{E\{\Delta t\}}{var\{\Delta t\}} = \frac{\overline{\Delta t}}{\sigma^2_{\Delta t}}$$

Here, $E\{\Delta t\} = \overline{\Delta t}$ denotes the mean, and $var\{\Delta t\} = \sigma^2_{\Delta t}$ is the variance of the interevent times. Alternatively, we can have a similar form based on the normalized interevent times, τ (where $\tau = \Delta t/\overline{t}$), relative to the mean value of a set of events (*41*):

$$p(\tau) = C' \cdot \tau^{\gamma'-1} \cdot \exp(\tau/\beta)$$

$$\frac{1}{\beta} = \frac{E\{\tau\}}{var\{\tau\}} = \frac{\overline{\tau}}{\sigma^2_\tau} = \frac{1}{\sigma^2_\tau} = \frac{\mu}{\lambda}$$

where λ is the total seismicity rate ($\lambda = 1/\Delta t$). Therefore, the dimensionless factor, $1/\beta$ encapsulates the fraction of non-clustered seismicity in the catalog, ranges from 0 to 1, generally. With $1/\beta = 1$, there are no triggered and temporally clustered earthquakes, and all events are non-clustered events; While $1/\beta = 0$ denotes all events are triggered and clustered seismicity as a pure aftershock sequence that follows Omori law would exhibit. Intermediate values in between represent the relative measure of non-clustered events activity in the catalog. Note that the branching ratio (the fraction of triggered events in a catalog) is just the fraction of non-clustered seismicity subtracted from one.

$$n = 1 - \frac{1}{\beta} \in [0, 1]$$

Therefore, by calculating the mean of interevent times over the variance of interevent times, we have an estimate of the non-clustered seismicity rate in the catalog. Further normalizing the non-clustered seismicity rate with respect to the total seismicity rate gives us the fraction of non-clustered events. Rather than relying on any particular triggering mechanism or declustering algorithm, this technique is robust given the seismicity catalog is complete. It only depends on

a simple metric of interevent times from a set of events, and magnitude is not considered into this formulation.

However, event subsets are not ideal under this framework if they deviate significantly from the general mixture of independent non-clustered events (Poisson point process) and triggered events (following the Omori law). For example, fitting a Gamma distribution to a perfect characteristic repeating earthquake sequence with exactly the same interevent times would result in a non-clustered rate of infinity, thus an infinite fraction of non-clustered events. Although observed repeater sequences rarely recur with an exactly constant time interval, the high periodicity of a repeater sequence can still result in a non-clustered event fraction larger than 1.0 based on this model, which is unphysical. A combination of many different repeating earthquake sequences (different interevent times) with many non-repeating events may be fine in adopting this framework. Also, event subsets with only aftershocks are also shown to give an overestimated non-clustered fraction (*32*).

Uncertainty of the estimates of the seismicity:

We use confidence intervals to present the uncertainty of estimates on seismicity properties. The 95% confidence interval of the non-clustered seismicity rate, the fraction of non-clustered seismicity, and the b-value presented in Fig. S4, are based on the bootstrapping method. We repeatedly and randomly resample the magnitude data for 10,000 times with replacement and calculate the b-value each time. We also repeatedly resample the interevent-time data with replacement and calculate the non-clustered seismicity rate and the fraction of non-clustered seismicity. For these 10,000 sets of sampling distributions, we take the 2.5^{th} and 97.5^{th} percentiles to represent the lower bound and the upper bound of the 95% confidence interval.

Supplementary Text

The non-clustered fractions in depth:

To better compare with fault slip models in two dimensions, we conduct the same analysis in along-strike and depth cells (Fig. S5). We apply the calculation of non-clustered fractions to cells on the fault plane with along-strike width of 2.5 km and a depth bin of 1.0 km. We omit the cells with less than 20 events. The histogram counting the number of events in depth is also binned into every 1 km.

The overall variation of the non-clustered fraction is consistent with the geodetic slip model (*28*), where both ends are strongly coupled at nearly all depths, and the middle section is weakly coupled. Limited by the seismicity distribution, we can only image the non-clustered fraction at a narrow width at depth (mostly from 4 km to 12 km depth).

The consistency surprisingly exists in detail. The southern transition has a small patch with a low non-clustered fraction at $\sim$195 km distance and 5–8 km depth (the cyan circle, A). This patch corresponds to an asperity inferred from the geodetic model (*28*) 8 km below Parkfield. In their model, a larger locked asperity has been inferred in the northern transition 40 km south of San Juan Bautista. This asperity aligns with an area with low non-clustered fraction at 75–90 km distance and 5–9 km depth (the purple circle, B). There is an asperity within the fast-creeping segment at a distance $\sim$135 km and 7–10 km depth (red circle, C) caused by the 2012 M5.3 event at 8.6 km depth. This patch is consistent with the geodetic model as well (*27, 28*).

The depth-dependent non-clustered fractions are also consistent with the previously observed microseismicity. The low non-clustered fractions within the north transition zone (the purple circle) could be linked to the localized clusters (Fig. 2b and c in the main text) of intense streaks of microearthquakes (*15, 28*). Yet, the paucity of events limits us from obtaining estimates on the fault plane with even finer resolution and reasonable uncertainties.

<u>The time-series of non-clustered fractions:</u>

This section corresponds to Fig. S6 of this document. To ensure having enough events for temporal analysis, we must sacrifice the spatial resolution with only four subsets of the entire

central SAF. The four subsets are: (1) the Loma Prieta segment; (2) the north transition zone; (3) the fast-creeping segment; (4) the south transition zone near Parkfield. The blue curves in Fig. S6 show the resulting time-series of the non-clustered fraction in four subsets, respectively. The length of the moving time window is fixed at two years, with a step of two months.

As explained in the main text, there are issues when dividing the catalogs into fine time windows due to a lack of events to fit a Gamma distribution of the interevent times properly. Marsan et. al. (*32*) proposed a better time-series analysis, which we did not pursue in our study. The basic idea is to adjust and extend the time windows adaptively to avoid only covering aftershocks.

The effect of cutoff magnitude:

The estimated magnitude of completeness in our entire catalog is about M1.5 (Fig. S2–S3). The interevent-time statistics below that cutoff magnitude is uncertain. Nevertheless, we can explore the influences of choosing different cutoffs by incrementally increasing the cutoff magnitude, M_c, and calculate the non-clustered fractions. The results are presented in Fig. S7 ($M_c = 2.0$) and Fig. S8 ($M_c = 2.5$). The general trend of non-clustered fractions along the fault does not change. The fractions still correlate well with the surface creep rate regardless of different cutoffs. But, by choosing a larger cutoff magnitude, the small aftershocks that are excluded outnumber the mainshocks (non-clustered events). Using a larger cutoff magnitude results in slightly higher values of non-clustered fractions, especially where small aftershocks are populated. Nevertheless, the main point here is that the non-clustered fraction is indicative to the coupling ratio. This conclusion is always obvious in the different magnitude ranges we tested.

The unreleased moment within the north transition zone:

The transition zone north of the central creeping section may have the potential to produce

large earthquakes based on the intermediate level of coupling, which motivates an investigation of the seismic moment release and accumulation. Assuming a conservative long-term plate motion of 34 mm/yr (*29, 66*) and the averaged interseismic creep rate at 8 km depth of $\sim$9.8 mm/yr (*28*) along the transition zone, there is a slip deficit of 2.4 cm/yr. From 1984 to present (37 years), this deficit corresponds to $3.0 \times 10^{19}\ N \cdot m$ of moment on a rectangular fault plane which is 75 km long and 15 km wide, given a shear modulus of 30 GPa. Based on our dataset, the released seismic moment by the seismicity within the transition zone adds up to only $3.3 \times 10^{17}\ N \cdot m$, which is nearly two orders of magnitude smaller than the moment deficit. The total unreleased moment for the north transition zone over 1984–2020 is equivalent to a M_w 7.0 earthquake.

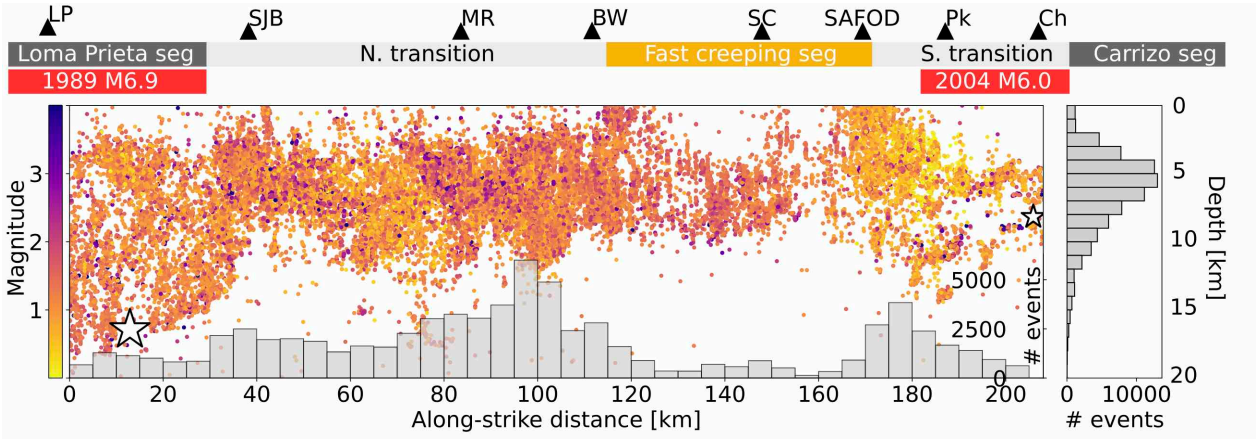

Fig. S1. Hypocenters of the seismicity along the central SAF. The color is coded by event magnitude. White stars mark the 1989 M6.9 Loma Prieta and the 2004 M6.0 Parkfield mainshock. Red bars marked the 1989 Loma Prieta and the 2004 Parkfield rupture extent, respectively. LP: Loma Prieta; SJB: San Juan Bautista; MR: Melendy Ranch; BW: Bitterwater; SC: Slack Canyon; SAFOD: San Andreas Fault Observatory at Depth; Pk: Parkfield; Ch: Cholame.

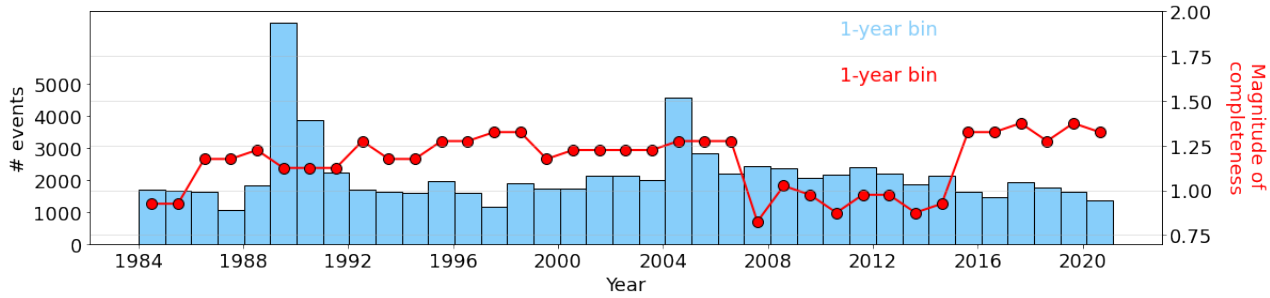

Fig. S2. Number of earthquakes each year from 1984 to 2021 (blue rectangles). The magnitude of completeness estimated from the MAXC method are plotted with red dots. The values of the magnitude of completeness range from 0.8–1.5. We thereby set a conservative minimum magnitude $M_{min} = 1.5$ for our entire analysis in this study.

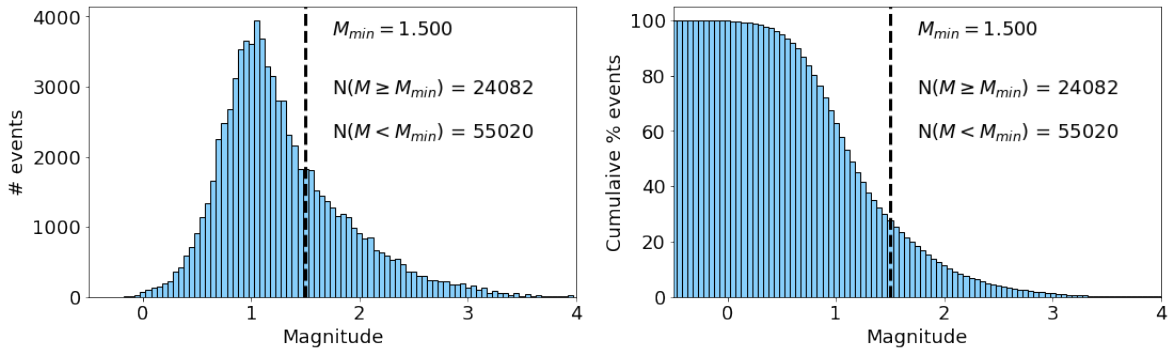

Fig. S3. Magnitude-frequency distribution of the earthquake catalog. Based on the assessment on the magnitude of completeness, we specify a minimum magnitude, $M_{min} = 1.5$, which gives us 24,082 events for our analysis over three decades from 1984 to 2021.

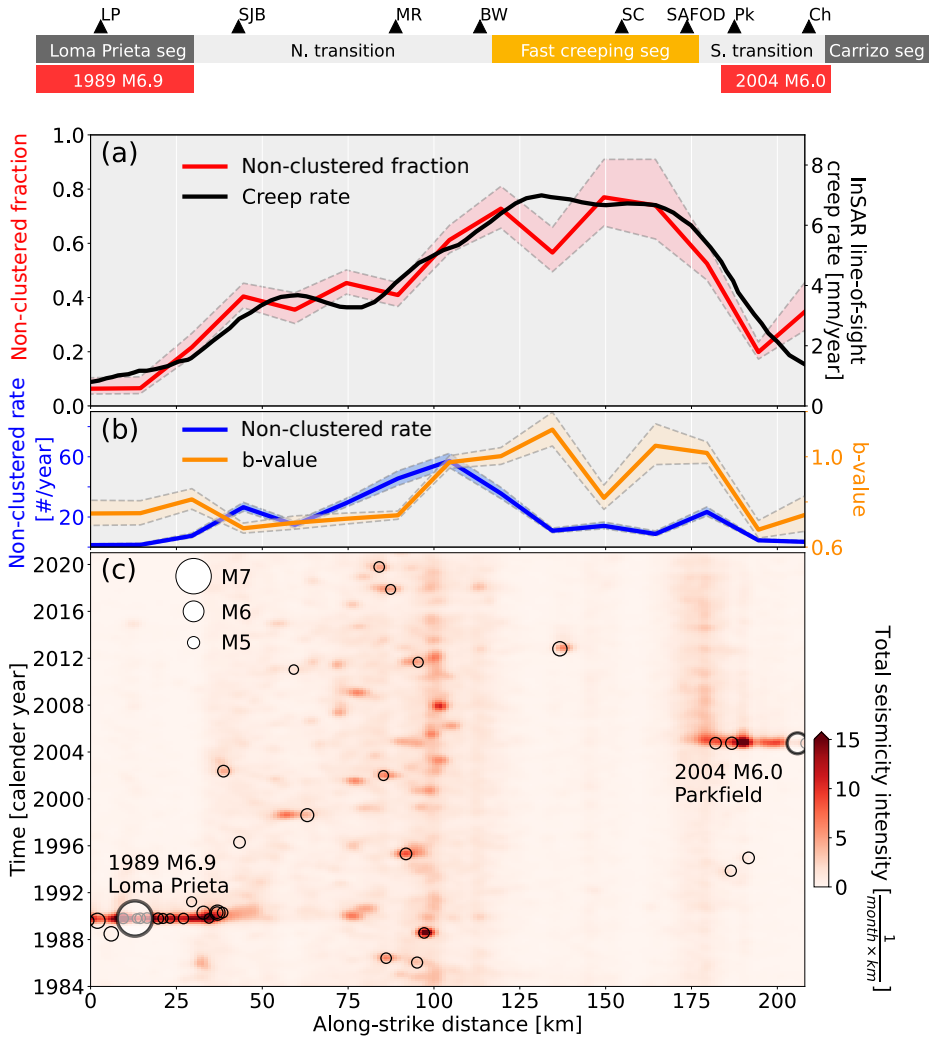

Fig. S4. Non-clustered fraction, non-clustered rate, b-value, and the seismicity intensity along the central SAF. Similar analysis to Fig. 2 of the main text. But the calculation here is only applied to 14 separate along-strike windows, each 15-km wide, rather than a sliding window as in Fig. 2. This is meant to show proper bootstrapping uncertainties with independent samples between spatial windows. The red, blue, and orange shading shows the 95% confidence interval of the estimates. See Supplementary Text in the section "Uncertainty of the estimates of the seismicity".

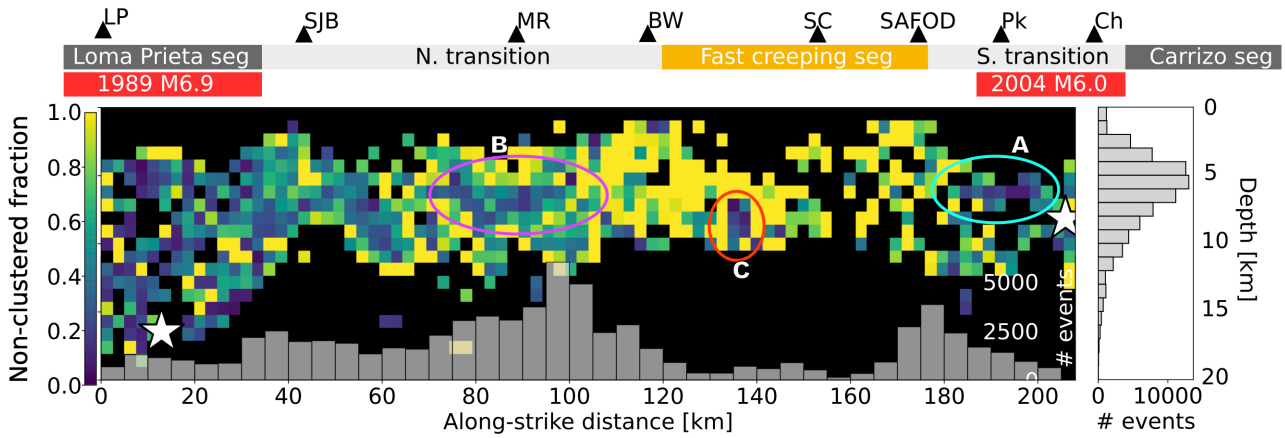

Fig. S5. Non-clustered fraction estimated on a regular along-strike (2.5 km) and depth (1.0 km) cells. The two white stars marked the hypocenters of the 1989 and the 2004 earthquakes. The grey histogram on the right shows the depth distribution of events. Cells containing less than 20 events are colored as black to avoid biased interpretation. The colored circles indicate the fault areas discussed in Supplementary Text in the section "The non-clustered fractions in depth".

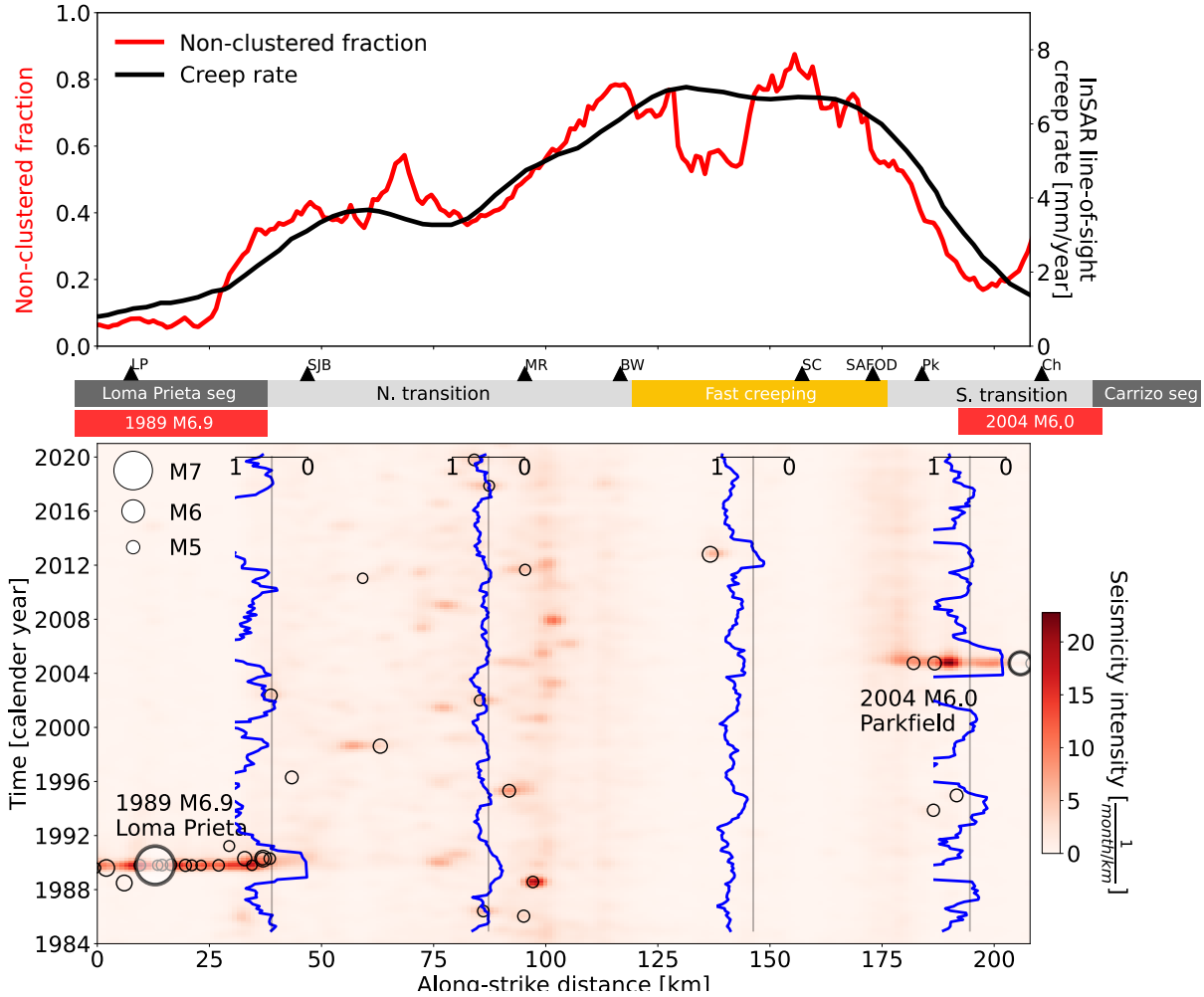

Fig. S6. The blue curves in the lower panel show the time-series of the non-clustered fractions. The length of the moving time window is two years, and the step size is two months. See Supplementary Text in the section "The time-series of non-clustered fractions".

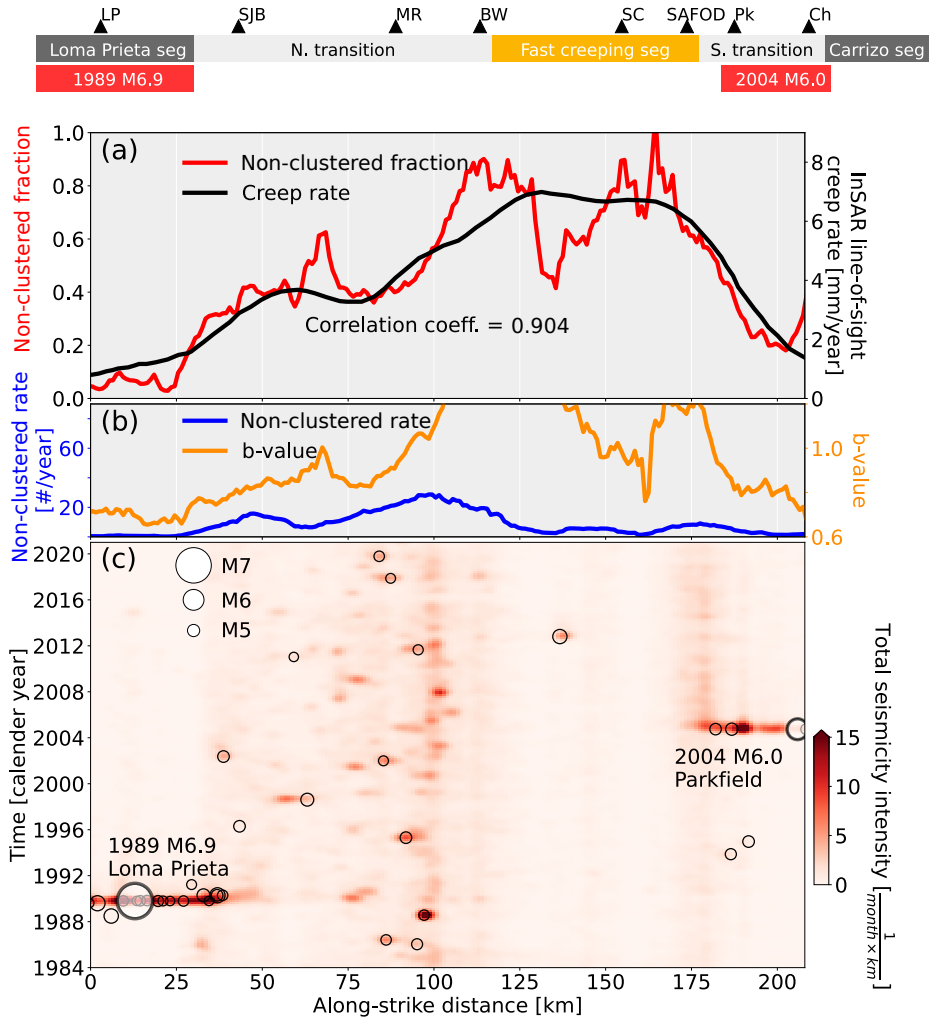

Fig. S7. Similar to Fig. S4. Analysis using a cutoff magnitude of M 2.0.

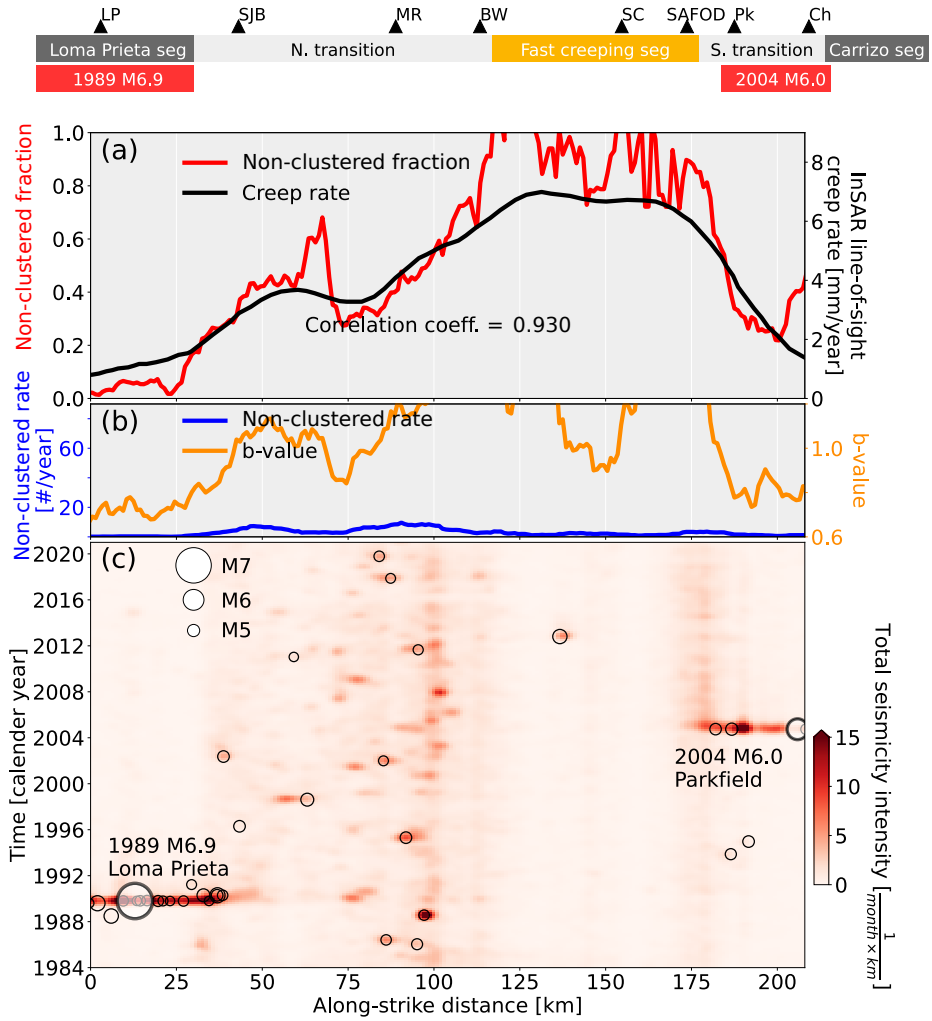

Fig. S8. Similar to Fig. S4. Analysis using a cutoff magnitude of M 2.5.

REFERENCES AND NOTES

1. C. O. Sanders, H. Kanamori, A seismotectonic analysis of the Anza Seismic Gap, San Jacinto Fault Zone, southern California. *J. Geophys. Res. Solid Earth* **89**, 5873–5890 (1984).

2. P. M. Shearer, Parallel fault strands at 9-km depth resolved on the Imperial Fault, Southern California. *Geophys. Res. Lett.* **29**, 19-1–19-4 (2002).

3. Z. E. Ross, E. Hauksson, Y. Ben-Zion, Abundant off-fault seismicity and orthogonal structures in the San Jacinto fault zone. *Sci. Adv.* **3**, e1601946 (2017).

4. N. Uchida, R. Bürgmann, Repeating earthquakes. *Annu. Rev. Earth Planet. Sci.* **47**, 305–332 (2019).

5. D. R. Shelly, Migrating tremors illuminate complex deformation beneath the seismogenic San Andreas fault. *Nature* **463**, 648–652 (2010).

6. H. Kanamori, E. E. Brodsky, The physics of earthquakes. *Rep. Prog. Phys.* **67**, 1429–1496 (2004).

7. Y. Ben-Zion, V. Lyakhovsky, Analysis of aftershocks in a lithospheric model with seismogenic zone governed by damage rheology. *Geophys. J. Int.* **165**, 197–210 (2006).

8. Y. Kaneko, J. P. Avouac, N. Lapusta, Towards inferring earthquake patterns from geodetic observations of interseismic coupling. *Nat. Geosci.* **3**, 363–369 (2010).

9. S. Barbot, N. Lapusta, J.-P. Avouac, Under the hood of the earthquake machine: Toward predictive modeling of the seismic cycle. *Science* **336**, 707–710 (2012).

10. R. Bürgmann, The geophysics, geology and mechanics of slow fault slip. *Earth Planet. Sci. Lett.* **495**, 112–134 (2018).

11. J. F. Pacheco, L. R. Sykes, C. H. Scholz, Nature of seismic coupling along simple plate boundaries of the subduction type. *J. Geophys. Res. Solid Earth* **98**, 14133–14159 (1993).

12. K. Wang, T. Dixon, "Coupling" Semantics and science in earthquake research. *EOS Trans. Am. Geophys. Union* **85**, 180 (2004).

13. J. P. Avouac, From geodetic imaging of seismic and aseismic fault slip to dynamic modeling of the seismic cycle. *Annu. Rev. Earth Planet. Sci.* **43**, 233–271 (2015).

14. F. Waldhauser, D. P. Schaff, Large-scale relocation of two decades of Northern California seismicity using cross-correlation and double-difference methods. *J. Geophys. Res. Solid Earth* **113**, B08311 (2008).

15. A. M. Rubin, D. Gillard, J. L. Got, Streaks of microearthquakes along creeping faults. *Nature* **400**, 635–641 (1999).

16. O. Zakharova, S. Hainzl, D. Lange, B. Enescu, Spatial variations of aftershock parameters and their relation to geodetic slip models for the 2010 Mw8.8 maule and the 2011 Mw9.0 Tohoku-oki earthquakes. *Pure Appl. Geophys.* **174**, 77–102 (2017).

17. S. Hainzl, C. Sippl, B. Schurr, Linear relationship between aftershock productivity and seismic coupling in the northern chile subduction zone. *J. Geophys. Res. Solid Earth* **124**, 8726–8738 (2019).

18. A. O. Konca, J. P. Avouac, A. Sladen, A. J. Meltzner, K. Sieh, P. Fang, Z. Li, J. Galetzka, J. Genrich, M. Chlieh, D. H. Natawidjaja, Y. Bock, E. J. Fielding, C. Ji, D. V. Helmberger, Partial rupture of a locked patch of the Sumatra megathrust during the 2007 earthquake sequence. *Nature* **456**, 631–635 (2008).

19. C. H. Scholz, Earthquakes and friction laws. *Nature* **391**, 37–42 (1998).

20. D. E. Moore, M. J. Rymer, Talc-bearing serpentinite and the creeping section of the San Andreas fault. *Nature* **448**, 795–797 (2007).

21. D. M. Saffer, L. M. Wallace, The frictional, hydrologic, metamorphic and thermal habitat of shallow slow earthquakes. *Nat. Geosci.* **8**, 594–600 (2015).

22. T. Sun, D. Saffer, S. Ellis, Mechanical and hydrological effects of seamount subduction on megathrust stress and slip. *Nat. Geosci.* **13**, 249–255 (2020).

23. W. F. Brace, J. D. Byerlee, Stick-slip as a mechanism for earthquakes. *Science* **153**, 990–992 (1966).

24. G. C. McLaskey, S. D. Glaser, Micromechanics of asperity rupture during laboratory stick slip experiments. *Geophys. Res. Lett.* **38**, L12302 (2011).

25. S. Ide, The proportionality between relative plate velocity and seismicity in subduction zones. *Nat. Geosci.* **6**, 780–784 (2013).

26. S. J. Titus, C. DeMets, B. Tikoff, Thirty-five-year creep rates for the creeping segment of the San Andreas fault and the effects of the 2004 Parkfield earthquake: Constraints from alignment arrays, continuous global positioning system, and creepmeters. *Bull. Seismol. Soc. Am.* **96**, S250-S268 (2006).

27. J. Maurer, K. Johnson, Fault coupling and potential for earthquakes on the creeping section of the central San Andreas Fault. *J. Geophys. Res. Solid Earth* **119**, 4414–4428 (2014).

28. R. Jolivet, M. Simons, P. S. Agram, Z. Duputel, Z. K. Shen, Aseismic slip and seismogenic coupling along the central San Andreas Fault. *Geophys. Res. Lett.* **42**, 297–306 (2015).

29. S. J. Titus, M. Dyson, C. De Mets, B. Tikoff, F. Rolandone, R. Bürgmann, Geologic versus geodetic deformation adjacent to the San Andreas fault, central California. *Bulletin* **123**, 794–820 (2011).

30. X. Tong, D. T. Sandwell, B. Smith-Konter, High-resolution interseismic velocity data along the San Andreas Fault from GPS and InSAR. *J. Geophys. Res. Solid Earth* **118**, 369–389 (2013).

31. D. Marsan, M. Bouchon, B. Gardonio, H. Perfettini, A. Socquet, B. Enescu, Change in seismicity along the Japan trench, 1990-2011, and its relationship with seismic coupling. *J. Geophys. Res. Solid Earth* **122**, 4645–4659 (2017).

32. D. Marsan, E. Prono, A. Helmstetter, Monitoring aseismic forcing in fault zones using earthquake time series. *Bull. Seismol. Soc. Am.* **103**, 169–179 (2013).

33. R. M. Nadeau, T. V. McEvilly, Periodic pulsing of characteristic microearthquakes on the San Andreas fault. *Science* **303**, 220–222 (2004).

34. J. Jiang, N. Lapusta, Deeper penetration of large earthquakes on seismically quiescent faults. *Science* **352**, 1293–1297 (2016).

35. P. Bird, Y. Y. Kagan, D. D. Jackson, F. P. Schoenberg, M. J. Werner, Linear and nonlinear relations between relative plate velocity and seismicity. *Bull. Seismol. Soc. Am.* **99**, 3099–3113 (2009).

36. N. Uchida, T. Matsuzawa, Pre- and postseismic slow slip surrounding the 2011 Tohoku-oki earthquake rupture. *Earth Planet. Sci. Lett.* **374**, 81–91 (2013).

37. W. Yang, Y. Ben-Zion, Observational analysis of correlations between aftershock productivities and regional conditions in the context of a damage rheology model. *Geophys. J. Int.* **177**, 481–490 (2009).

38. Y. Ben-Zion, C. G. Sammis, Characterization of fault zones. *Pure Appl. Geophys.* **160**, 677–715 (2003).

39. M. Khoshmanesh, M. Shirzaei, Episodic creep events on the San Andreas Fault caused by pore-pressure variations. *Nat. Geosci.* **11**, 610–614 (2018).

40. A. M. Thomas, R. M. Nadeau, R. Bürgmann, Tremor-tide correlations and near-lithostatic pore pressure on the deep San Andreas fault. *Nature* **462**, 1048–1051 (2009).

41. S. Hainzl, F. Scherbaum, C. Beauval, Estimating background activity based on interevent-time distribution. *Bull. Seismol. Soc. Am.* **96**, 313–320 (2006).

42. E. H. Field, R. J. Arrowsmith, G. P. Biasi, P. Bird, T. E. Dawson, K. R. Felzer, D. D. Jackson, K. M. Johnson, T. H. Jordan, C. Madden, A. J. Michael, K. R. Milner, M. T. Page, T. Parsons, P. M. Powers, B. E. Shaw, W. R. Thatcher, R. J. Weldon, Y. Zeng, Uniform California earthquake rupture forecast, version 3 (UCERF3)—The time-independent model. *Bull. Seismol. Soc. Am.* **104**, 1122–1180 (2014).

43. R. A. Harris, Large earthquakes and creeping faults. *Rev. Geophys.* **55**, 169–198 (2017).

44. Y. Ben-Zion, J. R. Rice, R. Dmowska, Interaction of the San Andreas Fault creeping segment with adjacent great rupture zones and earthquake recurrence at Parkfield. *J. Geophys. Res. Solid Earth* **98**, 2135–2144 (1993).

45. W. H. Bakun, B. Aagaard, B. Dost, W. L. Ellsworth, J. L. Hardebeck, R. A. Harris, C. Ji, M. J. S. Johnston, J. Langbein, J. J. Lienkaemper, A. J. Michael, J. R. Murray, R. M. Nadeau, P. A. Reasenberg, M. S. Reichle, E. A. Roeloffs, A. Shakal, R. W. Simpson, F. Waldhauser, Implications for prediction and hazard assessment from the 2004 Parkfield earthquake. *Nature* **437**, 969–974 (2005).

46. N. A. Toké, J. R. Arrowsmith (2013).

47. D. P. Schwartz, Review: Past and future fault rupture lengths in seismic source characterization—The long and short of it. *Bull. Seismol. Soc. Am.* **108**, 2493–2520 (2018).

48. H. Noda, N. Lapusta, Stable creeping fault segments can become destructive as a result of dynamic weakening. *Nature* **493**, 518–521 (2013).

49. I. Ryder, R. Bürgmann, Spatial variations in slip deficit on the central San Andreas Fault from InSAR. *Geophys. J. Int.* **175**, 837–852 (2008).

50. Y Ogata, Statistical models for earthquake occurrences and residual analysis for point processes. *J. Am. Stat. Assoc.* **83**, 9–27 (1988)

51. I. Zaliapin, Y. Ben-Zion, Earthquake clusters in southern California I: Identification and stability. *J. Geophys. Res. Solid Earth* **118**, 2847–2864 (2013).

52. G. Molchan, Interevent time distribution in seismicity: A theoretical approach. *Pure Appl. Geophys.* **162**, 1135–1150 (2005).

53. T. Utsu, Y. Ogata, R. S. Matsu'ura, The centenary of the omori formula for a decay law of aftershock activity. *J. Phys. Earth* **43**, 1–33 (1995).

54. J. Dieterich, A constitutive law for rate of earthquake production and its application to earthquake clustering. *J. Geophys. Res. Solid Earth* **99**, 2601–2618 (1994).

55. U.S. Geological Survey and California Geological Survey, Quaternary fault and fold database for the United States (2006).

56. D. P. Schaff, F. Waldhauser, Waveform cross-correlation-based differential travel-time measurements at the northern California seismic network. *Bull. Seismol. Soc. Am.* **95**, 2446–2461 (2005).

57. F. Waldhauser, Near-real-time double-difference event location using long-term seismic archives, with application to Northern California. *Bull. Seismol. Soc. Am.* **99**, 2736–2748 (2009).

58. K. E. Sieh, Slip along the San Andreas fault associated with the great 1857 earthquake. *Bull. Seismol. Soc. Am.* **68**, 1421–1448 (1978).

59. D. J. Wald, H. Kanamori, D. V. Helmberger, T. H. Heaton, Source study of the 1906 San Francisco earthquake. *Bull. Seismol. Soc. Am.* **83**, 981–1019 (1993).

60. S. Wiemer, M. Wyss, Minimum magnitude of completeness in earthquake catalogs: Examples from Alaska, the Western United States, and Japan. *Bull. Seismol. Soc. Am.* **90**, 859–869 (2000).

61. J. Woessner, S. Wiemer, Assessing the quality of earthquake catalogues: Estimating the magnitude of completeness and its uncertainty. *Bull. Seismol. Soc. Am.* **95**, 684–698 (2005).

62. K. Aki, Maximum likelihood estimate of b in the formula log10N=a-bm and its confidence limits. *Bull. Earthq. Res.* **43**, 237–239 (1965).

63. Y. Y. Kagan, L. Knopoff, Stochastic synthesis of earthquake catalogs. *J. Geophys. Res. Solid Earth* **86**, 2853–2862 (1981).

64. Y. Ogata, Seismicity analysis through point-process modeling: A review, in *Seismicity Patterns, Their Statistical Significance and Physical Meaning*, M. Wyss, K. Shimazaki, A. Ito, Eds. (Springer, 1999), pp. 471–507.

65. Á. Corral, Universal local versus unified global scaling laws in the statistics of seismicity. *Phys. A* **340**, 590–597 (2004).

66. K. E. Sieh, R. H. Jahns, Holocene activity of the San Andreas fault at Wallace Creek, California. *Geol. Soc. Am. Bull.* **95**, 883–896 (1984).